Check for updates

Phase and morphological control of MoO₃₋ₓ nanostructures for efficient cancer theragnosis therapy†

Bo Li,[a] Xin Wang,[a] Xiaoyu Wu,[a] Guanjie He,*[b] Ruoyu Xu,[c] Xinwu Lu,*[a] Feng Ryan Wang[c] and Ivan P. Parkin [ID] *[b]

Nanostructures of metal oxide semiconductors play significant roles in a variety of areas, such as biotherapy, pollutant treatment and energy storage and conversion. The molybdenum oxide (MoO₃₋ₓ) nanostructures have shown promising applications especially when used as photothermal treatment agents due to their relatively low cost, facile synthesis and low toxicity. However, the design and synthesis of efficient MoO₃₋ₓ nanomaterials with tunable phases and morphologies for theragnosis of tumors remains a challenge. In this work, hydrophilic MoO₃₋ₓ with controlled structures and phases was synthesized by a simple one-step hydrothermal process. The as-obtained MoO₂ nanoclusters showed a desirable size of ∼40 nm in diameter exhibiting unique properties as a theragnosis nanoplatform: (1) strong near-infrared absorption, which is due to oxygen vacancies of the nanoclusters, as proved by photoluminescence spectroscopy and X-ray photoelectron spectroscopy; (2) excellent photothermal performance with a photothermal conversion efficiency of up to 62.1%; and (3) the image response of X-ray computed tomography (CT) and infrared thermal imaging for simultaneous diagnosis of tumors. This study provided the facile synthetic strategy for controllable metal oxide semiconductors and promoted the development of metal oxides for theragnosis therapy of cancers.

Photothermal therapy (PTT) for cancer ablation has attracted great research interest recently as an alternative to traditional cancer treatments.[1–3] Nanostructured metal oxide semiconductors with controlled phases and morphologies have been extensively developed for various applications, such as catalysis,[4] energy storage[5–7] and biotherapy,[8,9] *etc*. Currently, metal oxide nanomaterials with oxygen vacancies in their crystal structures, such as WO₃₋ₓ[10,11] and MoO₃₋ₓ,[12,13] which possess a localized surface plasmon resonance (LSPR) phenomenon have demonstrated strong near-infrared (NIR, 700–1400 nm) absorption.[14] These properties combined with the deep penetration of NIR light through surface tissues makes these materials potentially very effective PTT agents.[15,16]

The MoO₃₋ₓ nanostructures have shown promising applications especially when used as PTT agents due to their relatively low cost, mild synthesis, excellent photothermal performance and low toxicity.[12,13,17] Remarkable achievements have been made for MoO₃₋ₓ around biomedical applications, especially as PTT agents, but there remain prominent challenges such as materials synthesis procedures, size-controlled MoO₃₋ₓ nanostructures and improvement of photothermal performance.[13,18] Facile fabrication of MoO₃₋ₓ nanostructures was first realized by Song *et al.*[17] They showed that complicated post treatments of hydrophobic and less biocompatible oleylamine molecules coated nanomaterials could be avoided. However, the sizes of the nanostructures are relatively large and not suitable for bioapplications. It is well-known that often particle sizes larger than 100 nm will accumulate in the vital organs, such as livers.[19] The hysteretic clearance of those materials from the organisms could cause serious toxicity and lead to long-term inflammatory response. Quantum dots of MoO₃₋ₓ were synthesized for use as photoacoustic imaging guided photothermal/photodynamic cancer treatment. However, quantum dots suffer from the disadvantage of shorter blood circulation time which is not in favor of the uptake of PTT agents by tumors.[12] All-in-One theragnosis nanomaterials exhibiting excellent photothermal performances as well as the ability to diagnose cancers has become a research hotspots. Molybdenum has strong X-ray attenuation which can be used in diagnostic applications such as X-ray computed tomography (CT) imaging.[20] To the best of our knowledge, there is no report related to one-step synthesis of MoO₃₋ₓ with suitable nanostructures for use as an effective CT and infrared thermal imaging guided PTT agents.

ªDepartment of Vascular Surgery, Shanghai Ninth People's Hospital, Shanghai JiaoTong University School of Medicine, Shanghai 200011, People's Republic of China. E-mail: luxinwu@shsmu.edu.cn
ᵇChristopher Ingold Laboratory, Department of Chemistry, University College London, London WC1H 0AJ, UK. E-mail: guanjie.he.14@ucl.ac.uk, i.p.parkin@ucl.ac.uk
ᶜDepartment of Chemical Engineering, University College London, London WC1E 7JE, UK

Herein, we rationally designed a facile one-step hydrothermal method to synthesize MoO_{3-x} materials with varied nanostructures (nanotubes, nanoflakes, nanoflowers and nanoclusters) by simply changing the temperature and reagents used in the reactions. The as-obtained self-assembled MoO_2 nanoclusters can be used as the highly efficient CT and infrared thermal imaging guided PTT agents for cancer treatment *in vivo*.

MoO_{3-x} nanostructures with tunable phases and morphologies were synthesized from one-step hydrothermal process by using ammonium molybdate tetrahydrate as the Mo source and polyethylene glycol 400 (PEG-400) as the reductant and the hydrophilic coating layer. The morphologies of the as-obtained materials were firstly investigated by scanning electron microscopy (SEM). By controlling the temperature of the reactions at 90, 120, 150 or 180 °C, different morphologies of MoO_{3-x} nanostructures *i.e.* nanocubes, nanoflakes, nanoflowers and nanoclusters could be obtained. At lower temperatures, the products are relatively large with the size of hundreds of nanometers to several micrometers (Fig. 1a–c) and are not suitable for PTT agents *in vivo*. To further detect the sizes of the MoO_{3-x} nanoclusters, high magnification SEM (Fig. 2a) and transmission electron microscopy (TEM; Fig. 2b) images were performed. The nanoclusters show a rough surface and the BET surface area is ~18 m^2 g^{-1} (Fig. S1†). The average size of nanoclusters observed from TEM was around 40 nm, while that of nanoclusters measured by dynamic light scattering (DLS) was around 80 nm (Fig. S2†), indicating that those nanoclusters were mostly individually dispersed in the aqueous solution, and had an appropriate size for use as a PTT agent. High resolution TEM (HRTEM) images showed a lattice spacing of 0.34 nm, which corresponds to the {11} facets of tugarinovite MoO_2. Further X-ray diffraction (XRD) patterns demonstrated that all peaks of the samples corresponded to standard MoO_2 (JCPDS No. 32-0671) with no unmatched
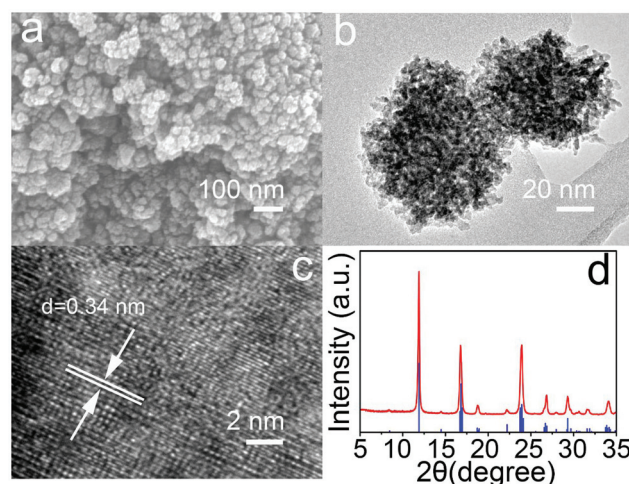

Fig. 2 (a) High magnification SEM images of MoO_2 nanoclusters; (b) TEM image, (c) high magnification TEM (HRTEM) image of MoO_2 nanoclusters; (d) XRD patterns of MoO_2 samples (blue index lines correspond to standard pattern JCPDS No. 32-0671).

peaks, indicating the sample is phase-pure. If PEG-400 is moving from the precursor solutions, MoO_{3-x} nanorods were obtained at all temperature ranges. Fig. S3† shows the representative morphology of MoO_{3-x} nanorods synthesized at 180 °C. XRD patterns (Fig. S4†) showed the MoO_{3-x} nanorods could be indexed to the molybdite structure of MoO_3 (JCPDS No. 35-0609). The structures of tugrinovite (MoO_2) and molybdite (MoO_3) are shown in Fig. S5a and 5b,† respectively. In both structures, the Mo atoms possess off-centre positions in the distorted MoO_6 octahedral. Hence, the coordination geometries of Mo are the same, Mo^{6+}. The compositions and the chemical states of MoO_2 nanoclusters and MoO_3 nanorods were detected and compared by X-ray photoelectron spectroscopy (XPS). Fig. S6† depicted the Mo 3d and O 1s spectra of MoO_2 and MoO_3 nanostructures, respectively. The curves of Mo 3d spectra can be fitted into two groups of spin–orbit doublets of MoO_2. The paired peaks at 233.9 and 231.0 eV can be attributed to Mo^{6+},[12] while the doublets at 232.8 and 229.6 eV are assigned to Mo^{4+}.[21] However, just one doublet (Fig. S6c†) from MoO_3 can be detected, which resulted from Mo^{6+}.[7] The major difference between the O 1s is at 532.6 eV, assigned to –OH in carbon chains from the hydrophilic modification by PEG-400 of MoO_2 nanoclusters.[22] In addition, the obvious peaks corresponded to oxygen vacancies in the matrix of metal oxides can be fitted to MoO_2 nanostructures, this was also proved by photoluminescence spectrum (Fig. S7†), which is the primary reason for LSPR phenomenon of transitional metal oxide materials.

It is well known that the surface chemistry of nanomaterials is very important for their biological application. Polyethylene glycol (PEG) is extensively applied to functionalize biomaterials to improve their dispersity and biocompatibility.[23,24] As a result, the PEG coated MoO_2 nanoclusters are hydrophilic without any modification, and they can well be dispersed in
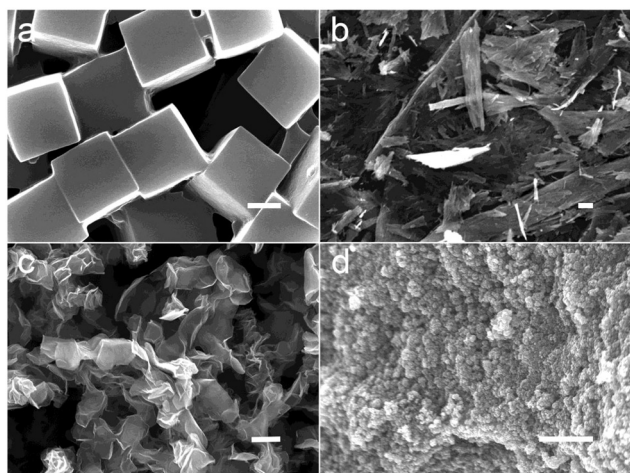

Fig. 1 SEM images of MoO_2 nanostructures synthesized from different temperatures (a) nanocubes; (b) nanoflakes; (c) nanoflowers and (d) nanoclusters. Scale bar: 1 μm.

water, saline, and RPMI-1640 culture medium without any noticeable agglomeration over a week (Fig. S8†) due to the small size and PEG coating. Then, UV-vis absorbance spectra were recorded for MoO_2 nanoclusters and MoO_3 nanorods. Shown in Fig. 3a, compared with MoO_3, MoO_2 nanoclusters presented stronger adsorption from 600–1000 nm with a peak maximum at 800 nm. Based on this light absorption character, an 808 nm laser was chosen to study the photothermal performance of MoO_2 nanoclusters. Under a continuous irradiation laser with a power density of 0.5 W cm^{-2}, the temperature of different concentration (0–500 ppm) of MoO_2 nanoclusters aqueous solutions was recorded. As shown in Fig. 3b and Fig. S9,† the nanoclusters exhibited concentration-dependent photothermal effects, as a control, the temperature of pure water showed little change (increase of 0.8 °C). The temperature increases of the MoO_2 nanoclusters aqueous dispersion change from 13.3 to 38.6 °C. We then measured the photothermal conversion efficiency of MoO_2 nanoclusters by a modified method similar to the reports on $Cu_{7.2}S_4$ nanocrystals.[25] According to the obtained date shown in Fig. 3b and Fig. S10,† the 808 nm laser heat conversion efficiency of MoO_2 nanoclusters can be calculated to be 62.1%, which is among the highest values in semiconductor materials as PTT, such as 28.1% for WO_{3-x} hierarchical nanostructures, 54.8% for RuO_2 nanoparticles,[26] 32.8% for WS_2 nanosheets,[27] and 22% for $Cu_{2-x}Se$ nanocrystals.[28] The high photothermal conversion

efficiency should be attributed to the strong NIR absorption resulted from the oxygen-deficiency-induced small polarons in MoO_2 nanoclusters and effective nonradiative electron relaxation dynamics,[29] as well as the special structure of MoO_2 nanoclusters which can serve as excellent laser-cavity mirrors of a 808 nm laser.[30] What's more, the as-prepared MoO_2 nanoclusters showed great NIR photostability without any significant decrease in the optical absorbance even upon a long time irradiation by a 2 W, 808 nm laser, whereas Au nanorods displayed notable changes in their optical properties (Fig. S11†). These results indicated that MoO_2 nanoclusters can be a promising 808 nm-laser-driven photothermal agent.

Prior to realizing the PTT *in vivo*, we evaluated the photothermal cytotoxicity of MoO_2 nanoclusters with and without laser irradiation on TC71 cells by CCK8 assay. These MoO_2 nanoclusters appeared to have low toxicity without NIR light irradiation. The cell viability was about 80% even at a high concentration up to 1000 ppm (Fig. S12a†). However, when simultaneously treatments with MoO_2 nanoclusters and 808 nm laser illumination (0.5 W cm^{-2}, 5 min), the cell viabilities significantly decreased as the concentration increased (Fig. S12b†). The *in vivo* therapeutic efficacy of the MoO_2 nanoclusters (250 ppm)-induced photothermal therapy cancer treatment using an 808 nm laser (0.5 W cm^{-2}) for 5 min was studied. All animal experiments were performed in accordance with the guidelines of the Institutional Animal Care and Use Committee of Shanghai JiaoTong University. The mice were randomly divided into four groups and then differently treated: (a) PBS solution, (b) MoO_2 nanoclusters, (c) MoO_2 nanoclusters + NIR laser 5 min, and (d) PBS + NIR laser 5 min. The mice from group (a) and (b) as a control were not irradiated, while the mice from group (c) and (d) were simultaneously exposed to an 808 nm laser. During the laser treatment, full-body infrared thermal images were captured using an IR camera. As shown in the inset of Fig. 3c, it can be clearly noticed that the region 11 framed area injected with the MoO_2 nanoclusters generates a greater temperature increase under irradiation, while, as a control, limited temperature change was detected in the region 12 framed area. The temperature of the irradiated area was also recorded as a function of the irradiation time (Fig. 3c). For the mouse injected with saline solution (region 12), the surface temperature of the tumor increased by less than 2 °C. However, in the case of the MoO_2 nanoclusters-injected mouse (region 11), the tumor surface temperature increased rapidly and reached up to 53.6 °C after 50 s, and then change to plateau at about 53.5 ± 0.7 °C. These results reveal a rapid elevation of temperature of the *in vivo* tumor, which suggests that the MoO_2 nanoclusters *in vivo* have an excellent photothermal effect. To further evaluate photothermal ablation of cancer cells *in vivo*, the histological examination of tumors was performed a day after treatments by means of microscopic imaging (Fig. 3d). As expected, significant cancer cell damage was noticed only in the tumor with both MoO_2 nanostructures injection and laser irradiation, but not in the three control groups. The experimental group shows severe cellular damage (pyknosis, karyorrhexis and karyolysis).
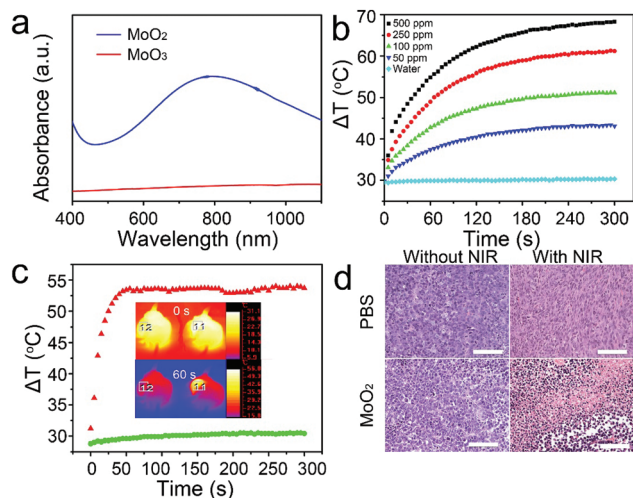

Fig. 3 (a) UV-vis absorbance spectra for the aqueous dispersion of the MoO_2 (blue line) and MoO_3 (red line) nanostructures synthesized at 180 °C. (b) Temperature elevation of the pure water and the aqueous dispersion of the MoO_2 nanoclusters with different concentrations under the irradiation of an 808 nm laser with a power density of 0.5 W cm^{-2} as a function of irradiation time (0–300 s). (c) The temperature profiles in region 11 and 12 as a function of the irradiation time. Insert: Infrared thermal images of two mice injected with the MoO_2 nanoclusters (the left mouse, indicated region 12) or saline (the right mouse, indicated region 11) *via* the hypodermic injection, respectively, irradiated with 808 nm laser (0.5 W cm^{-2}) at a time point of 0 and 60 s. (d) The representative hematoxylin and eosin stained histological images of the corresponding *ex vivo* tumor sections. Scale bar: 100 μm.

In the control groups, there are no obvious differences regarding the cells' size and shape, nuclear modifications, or necrosis. These facts suggest that *in vivo* cancer cells can be efficiently destroyed by the excellent photothermal effect of MoO_2 nanoclusters.

Fig. 4a presents the CT image of an aqueous dispersion of the MoO_2 nanoclusters at different concentrations. We can clearly observe that CT signal intensity is enhanced with an increase in the concentrations. Meanwhile, the Hounsfield Units (HU) values increased linearly with the concentration for the MoO_2 nanostructures as shown in Fig. 4b. The slope of the HU value was about 15.1 HU L g^{-1}. We then studied *in vivo* CT imaging using the MoO_2 nanostructures as a CT contrast agent. These MoO_2 nanoclusters dispersed in a PBS solution were intratumorally injected into a tumor-bearing mouse. Fig. 4c shows the *in vivo* tumor CT images before and after intratumoral injection with the MoO_2 solution (100 μL, 10 000 ppm). The corresponding injection site exhibited a brighter contrast than other soft tissues. Meanwhile, the mean CT value of the injection sites is much higher than the value of the soft tissues. The CT value of the tumor area post-injection was significantly higher than that of the tumor area before injection (a mean value: 147 *versus* 15). Therefore, these results obviously indicated that the MoO_2 nanostructures can be a promising CT contrast agent *in vivo*.

In conclusion, by controlling the reductants and reaction temperature in the hydrothermal synthesis, various phases and morphologies of MoO_{3-x} nanostructures can be synthesized. MoO_2 nanoclusters obtained at 180 °C have a size of 40 nm and can be used for bioapplications. Due to the intense NIR absorption and high photothermal conversion of 62.1%, MoO_2 nanoclusters were used as the PTT agents to kill cancer cells *in vitro* and *in vivo* efficiently under the irradiation of an 808 nm laser at a safe intensity of 0.5 W cm^{-2}. In addition, the CT response are reported for the first time of this kind of metal oxides. Therefore, MoO_2 nanoclusters are promising candidates for theragnosis therapy of cancers.
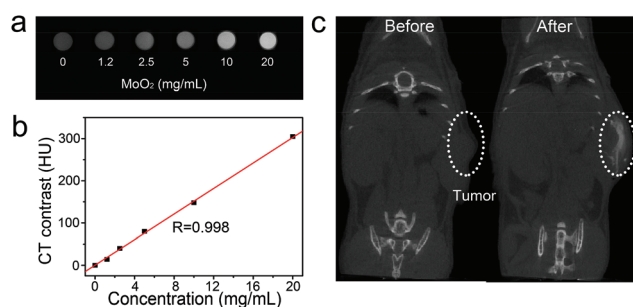

Fig. 4 (a) *In vitro* CT image of the MoO_2 nanostructures with different aqueous dispersion concentrations; (b) CT value (HU) of the MoO_2 nanostructures as a function of the concentration of nanostructures; (c) *In vivo* CT coronal views of a mouse following intratumoral injection of the solution with the MoO_2 nanostructures. The position of tumor is marked by white circles.

References

1 V. Biju, *Chem. Soc. Rev.*, 2014, **43**, 744–764.
2 Q. Chen, J. Wen, H. Li, Y. Xu, F. Liu and S. Sun, *Biomaterials*, 2016, **106**, 144–166.
3 M. Lan, S. Zhao, Z. Zhang, L. Yan, L. Guo, G. Niu, J. Zhang, J. Zhao, H. Zhang, P. Wang, G. Zhu, C. Lee and W. Zhang, *Nano Res.*, 2017, DOI: 10.1007/s12274-017-1528-0.
4 B. Liu, L. France, C. Wu, Z. Jiang, V. L. Kuznetsov, H. A. Al-Megren, M. Al-Kinany, S. A. Aldrees, T. Xiao and P. P. Edwards, *Chem. Sci.*, 2015, **6**, 5152–5163.
5 G. He, X. Han, R. Zou, T. Zhao, Z. Weng, S. Ho-Kimura, Y. Lu, H. Wang, Z. X. Guo and I. P. Parkin, *Adv. Funct. Mater.*, 2017, **27**, 1604903.
6 G. He, M. Qiao, W. Li, Y. Lu, T. Zhao, R. Zou, B. Li, J. A. Darr, J. Hu, M.-M. Titirici and I. P. Parkin, *Adv. Sci.*, 2017, **4**, 1600214.
7 H. S. Kim, J. B. Cook, H. Lin, J. S. Ko, S. H. Tolbert, V. Ozolins and B. Dunn, *Nat. Mater.*, 2017, **16**, 454–460.
8 A. Kumar, S. Kim and J.-M. Nam, *J. Am. Chem. Soc.*, 2016, **138**, 14509–14525.
9 C. Liang, L. Xu, G. Song and Z. Liu, *Chem. Soc. Rev.*, 2016, **45**, 6250–6269.
10 J. Liu, J. Han, Z. Kang, R. Golamaully, N. Xu, H. Li and X. Han, *Nanoscale*, 2014, **6**, 5770–5776.
11 L. Wen, L. Chen, S. Zheng, J. Zeng, G. Duan, Y. Wang, G. Wang, Z. Chai, Z. Li and M. Gao, *Adv. Mater.*, 2016, **28**, 5072–5079.
12 D. Ding, W. Guo, C. Guo, J. Sun, N. Zheng, F. Wang, M. Yan and S. Liu, *Nanoscale*, 2017, **9**, 2020–2029.
13 Q. Liu, C. Sun, Q. He, D. Liu, A. Khalil, T. Xiang, Z. Wu, J. Wang and L. Song, *Chem. Commun.*, 2015, **51**, 10054–10057.
14 B. Li, Y. Zhang, R. Zou, Q. Wang, B. Zhang, L. An, F. Yin, Y. Hua and J. Hu, *Dalton Trans.*, 2014, **43**, 6244–6250.
15 G. Ku, M. Zhou, S. Song, Q. Huang, J. Hazle and C. Li, *ACS Nano*, 2012, **6**, 7489–7496.
16 S. Zhao, G. Niu, F. Wu, L. Yan, H. Zhang, J. Zhao, L. Zeng and M. Lan, *J. Mater. Chem. B*, 2017, **5**, 3651–3657.
17 G. Song, J. Shen, F. Jiang, R. Hu, W. Li, L. An, R. Zou, Z. Chen, Z. Qin and J. Hu, *ACS Appl. Mater. Interfaces*, 2014, **6**, 3915–3922.
18 Y. Mao, W. Li, X. Sun, Y. Ma, J. Xia, Y. Zhao, X. Lu, J. Gan, Z. Liu, J. Chen, P. Liu and Y. Tong, *CrystEngComm*, 2012, **14**, 1419–1424.

19 B. Li, K. Ye, Y. Zhang, J. Qin, R. Zou, K. Xu, X. Huang, Z. Xiao, W. Zhang, X. Lu and J. Hu, *Adv. Mater.*, 2015, **27**, 1339–1345.

20 W. Yin, L. Yan, J. Yu, G. Tian, L. Zhou, X. Zheng, X. Zhang, Y. Yong, J. Li, Z. Gu and Y. Zhao, *ACS Nano*, 2014, **8**, 6922–6933.

21 J. Park, I. Choi, M. J. Lee, M. H. Kim, T. Lim, K. H. Park, J. Jang, S. M. Oh, S. K. Cho and J. J. Kim, *Electrochim. Acta*, 2014, **132**, 338–346.

22 C. D. Wagner, *Anal. Chem.*, 1980, **52**, 1445–1451.

23 K. Yang, L. Z. Feng, X. Z. Shi and Z. Liu, *Chem. Soc. Rev.*, 2013, **42**, 530–547.

24 Z. G. Chen, Q. Wang, H. L. Wang, L. S. Zhang, G. S. Song, L. L. Song, J. Q. Hu, H. Z. Wang, J. S. Liu, M. F. Zhu and D. Y. Zhao, *Adv. Mater.*, 2013, **25**, 2095–2100.

25 B. Li, Q. Wang, R. Zou, X. Liu, K. Xu, W. Li and J. Hu, *Nanoscale*, 2014, **6**, 3274–3282.

26 Z. Xiao, X. Jiang, B. Li, X. Liu, X. Huang, Y. Zhang, Q. Ren, J. Luo, Z. Qin and J. Hu, *Nanoscale*, 2015, **7**, 11962–11970.

27 Y. Yong, L. Zhou, Z. Gu, L. Yan, G. Tian, X. Zheng, X. Liu, X. Zhang, J. Shi, W. Cong, W. Yin and Y. Zhao, *Nanoscale*, 2014, **6**, 10394–10403.

28 C. M. Hessel, V. P. Pattani, M. Rasch, M. G. Panthani, B. Koo, J. W. Tunnell and B. A. Korgel, *Nano Lett.*, 2011, **11**, 2560–2566.

29 S. Link and M. A. El-Sayed, *Int. Rev. Phys. Chem.*, 2000, **19**, 409–453.

30 Q. W. Tian, M. H. Tang, Y. G. Sun, R. J. Zou, Z. G. Chen, M. F. Zhu, S. P. Yang, J. L. Wang, J. H. Wang and J. Q. Hu, *Adv. Mater.*, 2011, **23**, 3542–3547.